Electronic Supplementary Material (ESI) for Journal of Materials Chemistry A.

Supporting Information

Intrinsically Zwitter-ionic COF: Carboxylic Acid and Pseudo-tetrahedral *sp*^{3} Nitrogen Functionalized Covalent Organic Framework with Potential for Humidity Sensing

Shyamapada Nandi,*[a],¥ Himan Dev Singh,[b],¥ Pragalbh Shekhar,[b] Debanjan Chakraborty,[b] Rinku Kushwaha [b] and Ramanathan Vaidhyanathan*[b][c]

Contents:

1. Material and Methods:

Synthesis of tris[4-formylphenyl]amine:

The trialdehyde, tris[4-formylphenyl]amine was synthesized according to our earlier method.[S1]

Synthesis of IISERP-COF31:

Tris[4-formylphenyl]amine (0.25 mmol) and 3,5-diaminobenzoic acid (0.37 mmol) were added in a pyrex tube and dissolved in 2ml mesitylene, 3 ml o-dichlorobenzene and 4 ml ethanol. 0.25 ml acetic acid was added to this mixture and was stirred well. The pyrex tube was then flash frozen using liquid nitrogen and sealed. The contents in the sealed tube was heated at 120°C for 3 days. After cooling to room temperature, the light yellow precipitate was filtered and washed with DMF, THF, MeOH. Yield (76%), Formula for COF $C_{63}H_{42}N_8O_6$ (**1**), M. Wt. 1007.06 g/mol, CHN Observed is C = 75.14; H = 4.20; N = 11.13. Calc. C = 72.65; H = 3.53; N = 13.36.

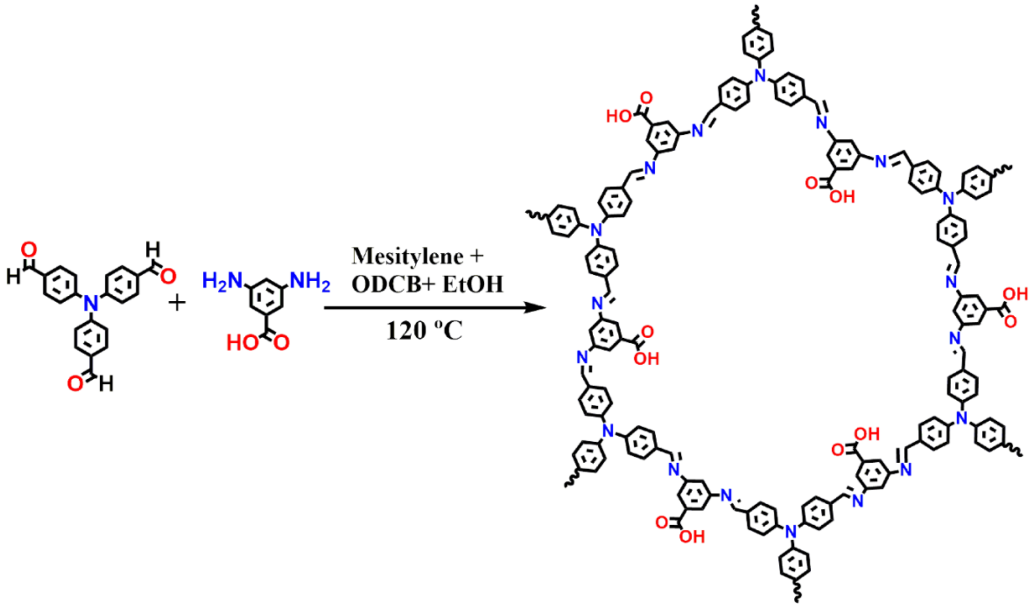

Scheme 1: Schematic diagram of the COF synthesis with details of the procedure.

2. Analytical characterization:

Powder X-ray diffraction:

Powder X-Ray has been carried out using a Rigaku Miniflex benchtop instrument with a Cu Kα (λ = 1.541 Å) source and the data were processed using PDXL software. In some cases, the data was collected using a Bruker D8 venture instrument.

Thermo gravimetric Analysis:

NETSZCH TGA-DSC instrument has been used for TGA analysis. The sample was heated under N_2 flow of 20 ml/min (purge + protective) from 25°C to 600°C with a heating rate of 5 K/min.

Infra-Red spectroscopy (IR):

IR spectra were obtained using a Nicolet ID5 attenuated total reflectance IR spectrometer in a range of 4000-600 cm^{-1}. KBr pellets were made with the sample to record IR.

Nuclear Magnetic Resonance spectroscopy (NMR):

Solid state magic angle spinning NMR spectra for COF was recorded using Bruker 500 MHz NMR spectrometer.

Field Emission-SEM:

Ultra Plus Field Emission Scanning Electron Microscope with integral charge compensator and embedded EsB and AsB detectors was used for recording the SEM images and EDX analysis. During sample preparation, the solid samples were dispersed in THF and sonicated for 10 mins. The dispersed samples were drop casted on silicon wafer and dried in a vacuum oven for overnight.

HR-Transmission electron microscopy (HRTEM):

FEI (Jeol FEG 2100F is the model) high-resolution transmission electron microscope (HR-TEM) equipped with a field emission source operating at 300 KeV was used for collecting the TEM images. The well dispersed sample was drop casted on a Cu grid and air dried.

XPS measurements:

XPS measurements were carried out using Thermo Kalpha+ spectrometer using micro focused and monochromated AlKα radiation with energy 1486.6 eV. The base pressure of the spectrometer was better than 10^{-8} mbar during the spectral acquisition. The pass energy for spectral acquisition was kept at 50 eV for individual core-levels. The electron flood gun was utilized for providing charge compensation during data acquisition. The peak fitting of the individual core-levels were done using XPS peak software with a Shirley type background.

Adsorption studies:

All the adsorptions were performed using a Micromeritics 3-FLEX pore and surface area analyzer and in few cases using Micromeritics ASAP 2020 HD instrument. Water adsorption was performed on Micromeritics ASAP 2020 HD. In each case, prior to the adsorption measurements, the powder sample was activated at 150°C under vacuum for 6 hours.

Solid State UV – vis spectroscopy:

Diffused reflectance spectra of microcrystalline powders in the UV−visible region are recorded using a Shimadzu UV-3600 plus UV−vis−NIR spectrophotometer. Then Kubelka-

Munk transformation is used for the analysis of diffuse reflectance spectra. It relates the reflectance data with absorption coefficient as in equation (1):

$F(R) = \alpha/S = (1\text{-}R)^2 /2R$…………………………………………………(1)

where F(R) is the Kubelka-Munk function, R is reflectance, α is absorption coefficient and S is the scattering factor.

Photoluminescence spectroscopy:

Steady-state photoluminescence (PL) and PL Excitation (PLE) are measured using Edinburgh FLS980 Instrument. Xenon lamp is used for steady state PL and PLE measurements.

3. Structure solution and modeling details:

All calculations were performed using the different packages implemented in the Materials Studio V8 (Accelrys Program). Simulation of the lowest energy structural configuration: An initial structure was developed via atomic-simulation in a hexagonal setting. The presence of the carboxylic acid groups on the linker diamines and the tetrahedral sp^3 center on the trialdehyde monomer, rendered the structure as buckled setting down into a low symmetry, P1. Both the eclipsed and staggered configurations were modeled and their corresponding PXRD patterns were simulated. The comparison of the simulated PXRDs against the experimental PXRD revealed that both the eclipsed and the staggered configuration matched better (Figure S4). However, the relative intensities of the staggred matched better also the staggered model better explains the experimentally observed porosity (experimental: 8-13 Å). Hence considering this configuration to be the initial model, we did a thorough geometry optimization using the DFTB+ routine, recommended for periodic structures (see below for the parameters). The optimized structure was refined against the experimental powder pattern using the Pawley methods embedded in the Reflex model. This refined structure was used in all other calculations.

DFT geometry optimization using DFTB+: Once the initial configuration was decided, it was geometry optimized using DFTB+ acknowledged as an appropriate package for modelling periodic structures (*Th. Frauenheim et al., Atomistic simulations of complex materials: ground state and excited-state properties, J. Phys. Cond. Matter,* ***14****, 3015 (2002)*). ***Optimization parameters:*** The atomic parameterization was chosen from the CHNO parameter set available with the Slater-Koster library. Both positions and cells were optimized without any constraints using the Smart Algorithm. The final unit cell was triclinic, and its lattice parameters were just a short distance from the initial hexagonal lattice. In all cases, excellent convergence was achieved within a few SCC cycles. We used the Qeq charge equilibration method to fix the framework charges. All calculations were dispersion corrected using the Universal forcefield, including bond order assignment and spin-unrestricted, considering the formal spin as initial. The Hamiltonian diagonalizations were achieved using the Divide and Conquer Eigensolver. Broyden mixing scheme were used. A SCC tolerance was kept at 1 e-008 for all optimizations (*Q. Cui, M. Elstner, Th. Frauenheim, E. Kaxiras, M. Karplus, Combined self-consistent charge density functional tight-binding (SCC-DFTB) and CHARMM, J. Phys. Chem. B, 105, 569 (2001)*). A smearing parameter of 0.01 Ha was employed. The total energy/eigen energy tolerance was kept high at a value of 0.5×10^{-6} eV.

The total energy of the refined IISERP-COF31's structure stabilized at -204878.115861 kcal/mol at 0K for the staggred model and at -91338.4966975 kcal/molfor the eclipsed model. Thus, the former has significantly lowered relative energy as there are more interlayer interactions between the buckled layers.

Note: The table listing the atomic coordinates of the staggered model is provided as separate supporting document.

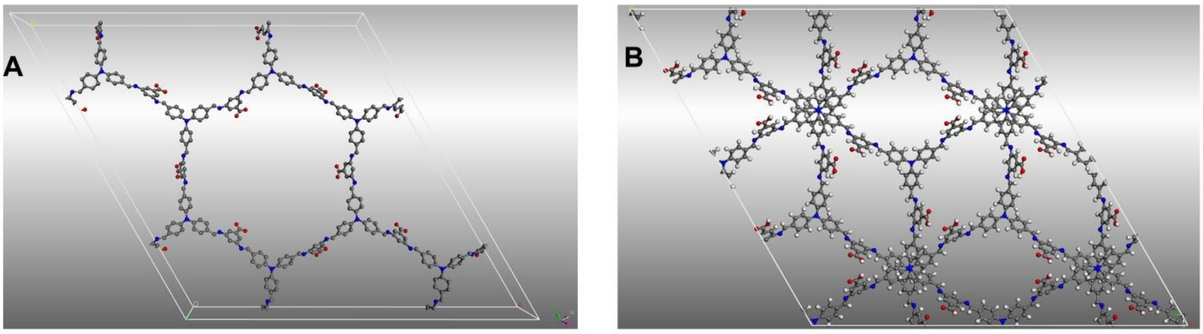

Figure S1. Modeled strucutre of the IISERP-COF31's eclipsed and staggered configuations.

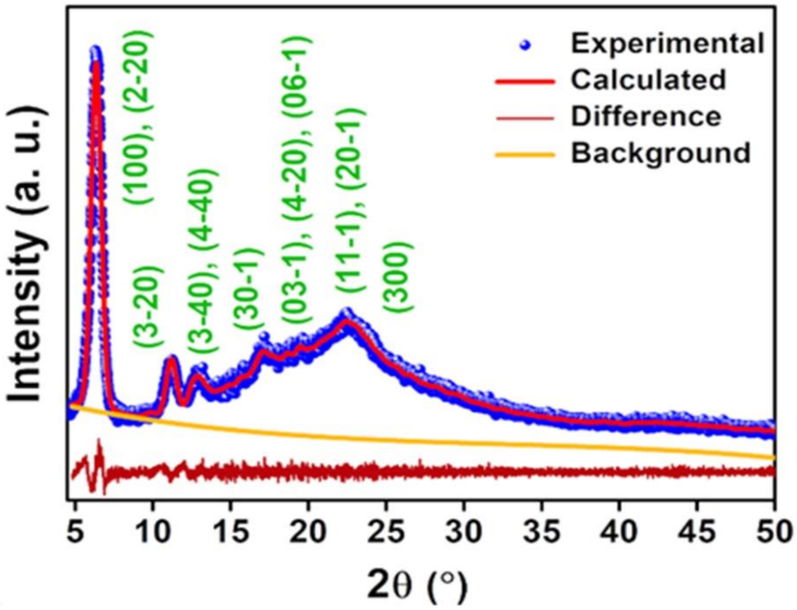

Figure S2. A fit from the Pawley refinement of the experimental powder pattern using the eclipsed model. Note: this is as good as the staggered configuration shown in Figure 2 of the main text. However, this eclipsed model does not explain the observed pore sizes.

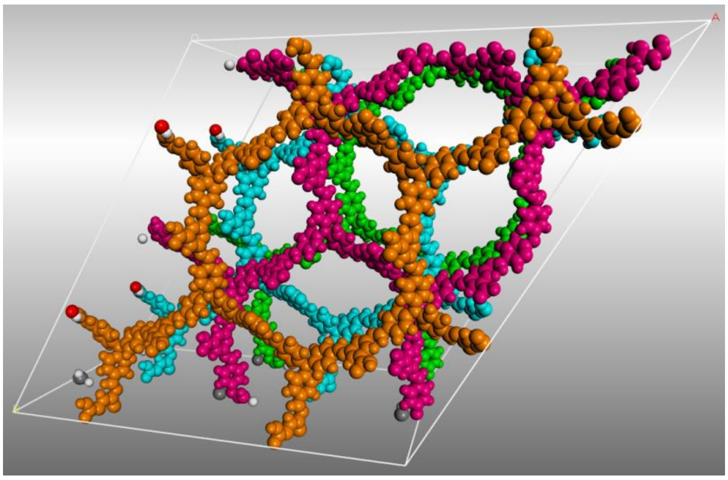

Figure S3. A 2 x 2 x 2 supercell of the staggered configuration showing the *ABAB*... stacking and the buckled layers give a psuedo 3D pore-structure**.**

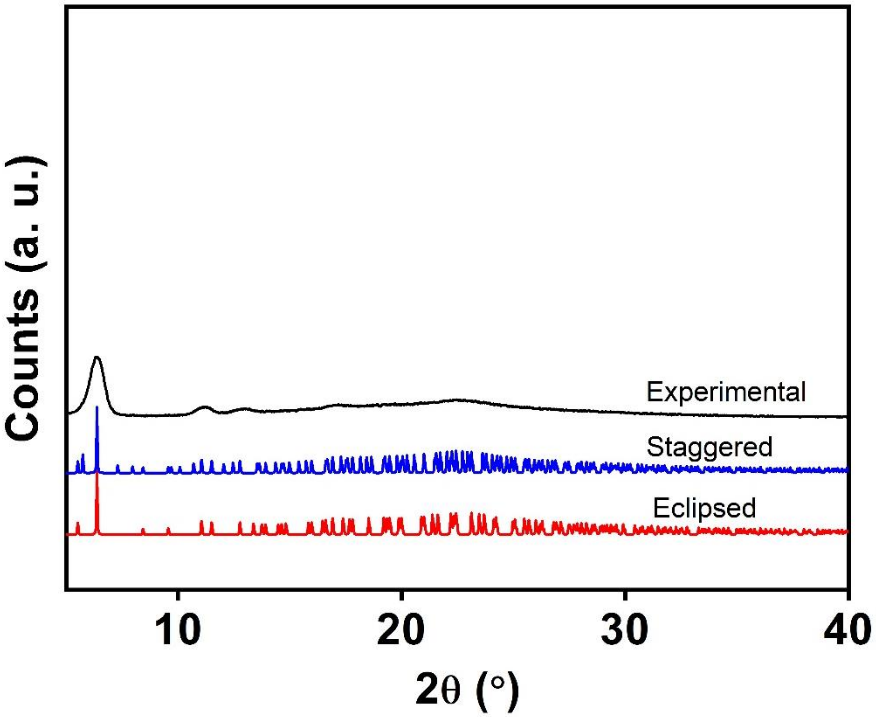

Figure S4. A comparative PXRD plot for **1**. Note the experimental PXRD matches with the simulated pattern in case of slipped layer conformation. This also matches well with the experimental porosity data.

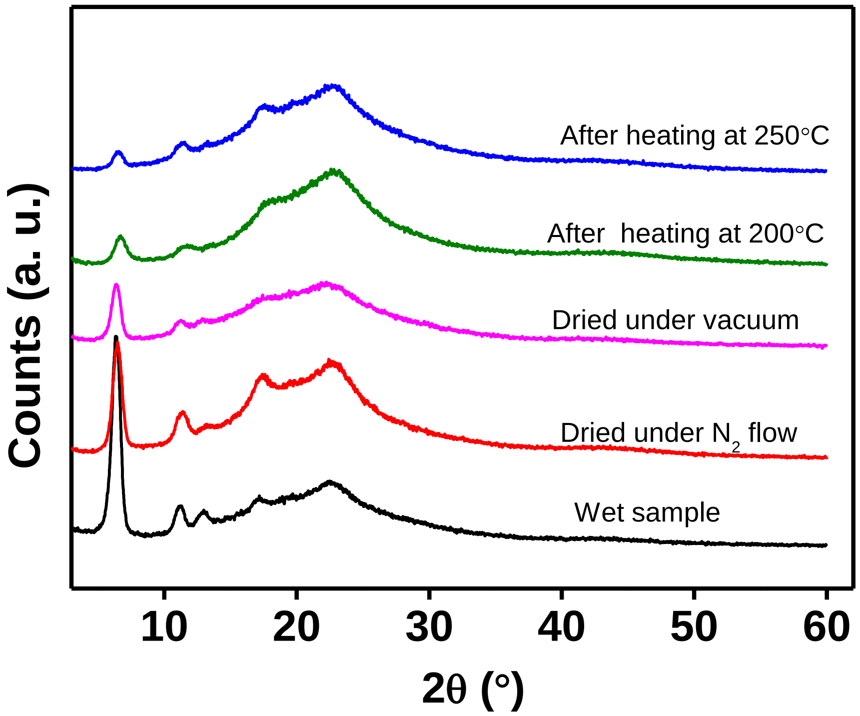

Figure S5. PXRD pattern of **1** under different conditions. Note: The wet sample (the sample was collected directly from the synthesis tube with small amount of solvent in order to avoid the exposure to humidity) and the N_2 dried sample was not exposed to atmosphere before the diffraction experiment. However, the other samples were exposed to atmosphere before drying.

4. Characterizations:

Thermo Gravimetric Analysis:

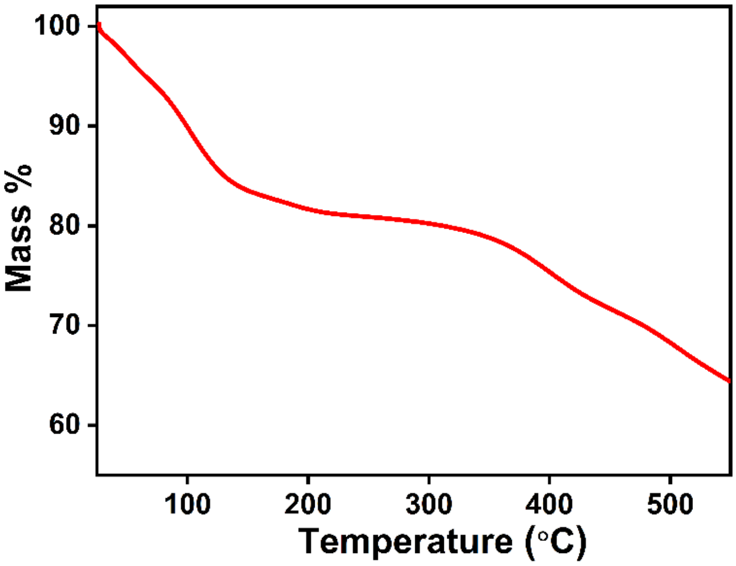

Figure S6. TGA plot of **1** showing the thermal stability up to 350°C. Initial weight loss is due to the solvents occluded in the COF pores.

Solid State Nuclear Magnetic Resonance Spectroscopy (SSNMR):

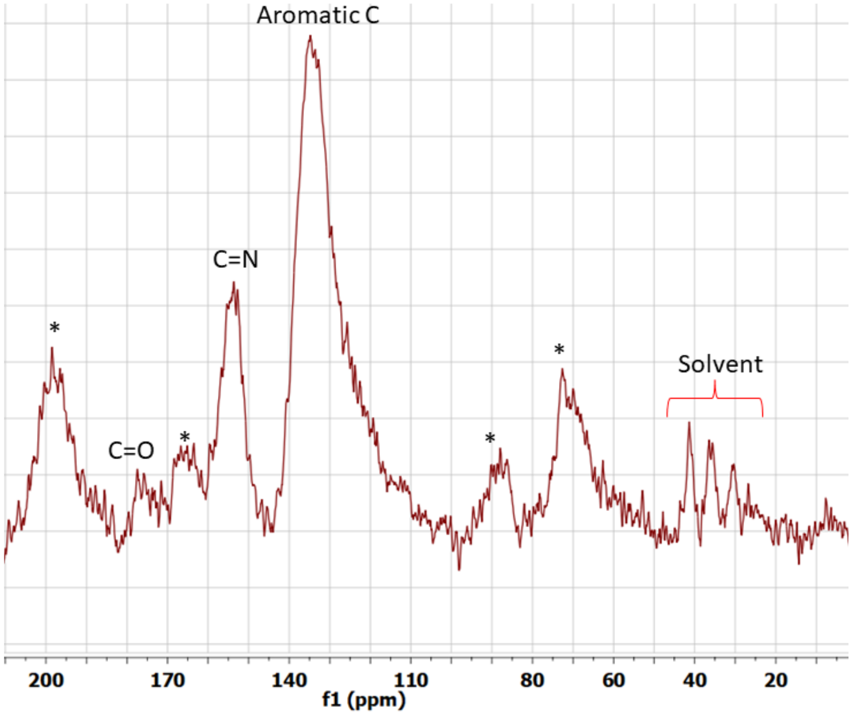

Figure S7. Solid state magic angle spinning NMR of **1** showing the characteristic signal due to C=N, C=O, C=C (aromatic backbone). The * represent the spinning side bands. Peak at 25-40 ppm is due to occluded solvents in the COF.

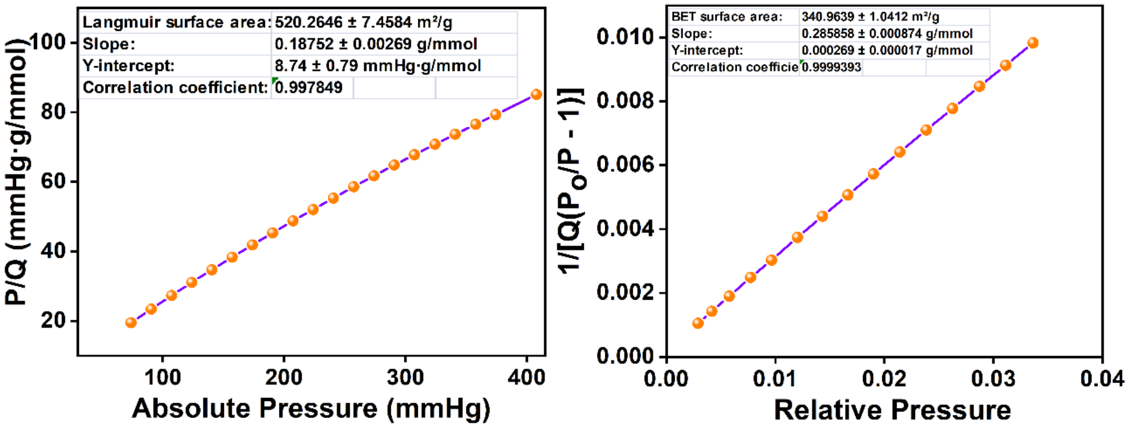

Figure S8. (Left) Langmuir surface area plot for **1**. (Right) Brunauer–Emmett–Teller surface area plot for **1**. These were estimated from the 77K N_2 isotherm.

Microscopic studies:

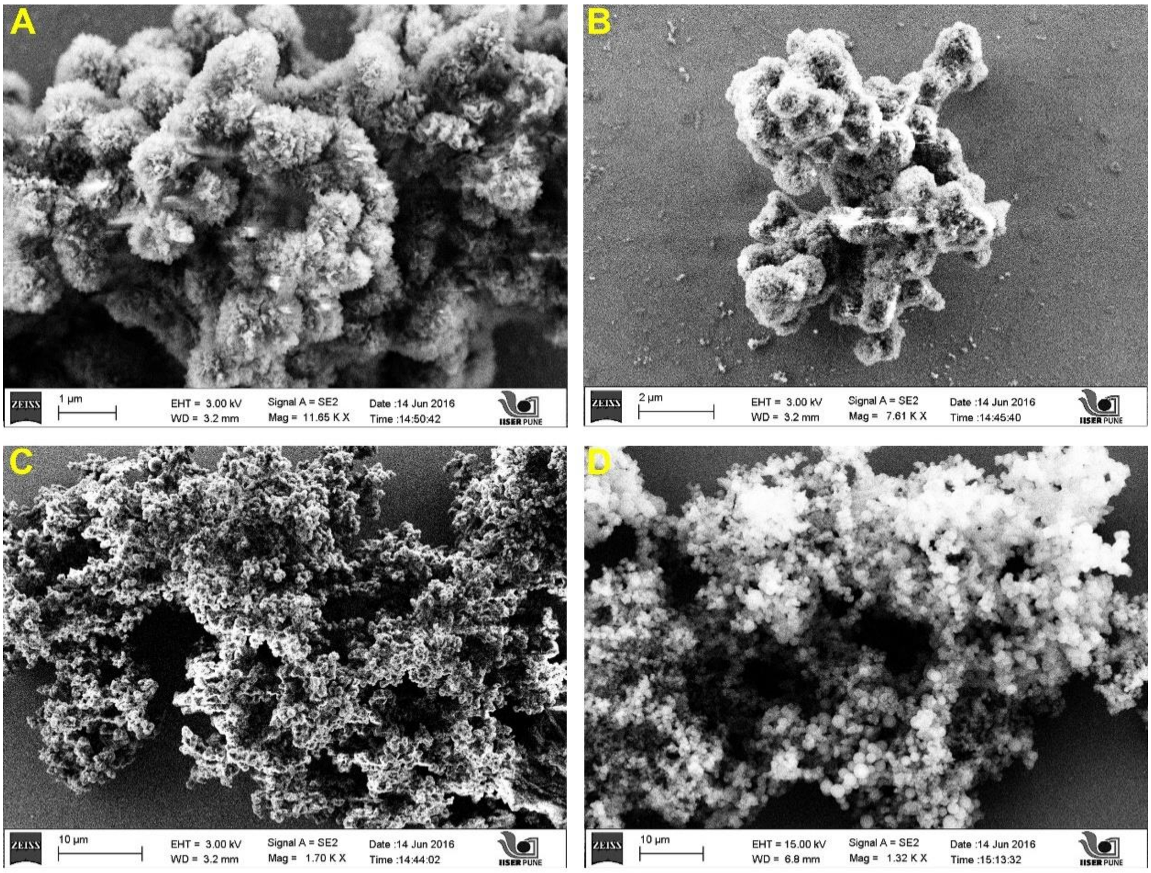

Figure S9. Scanning Electron Microscopic images of **1** under different magnifications.

Element	Weight%	Atomic%
C K	74.18	78.51
N K	8.63	7.83
O K	17.19	13.66
Totals	100.00	

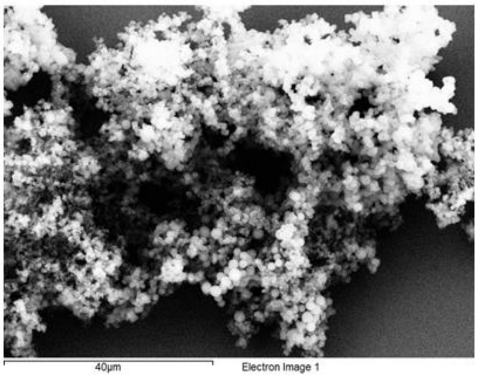

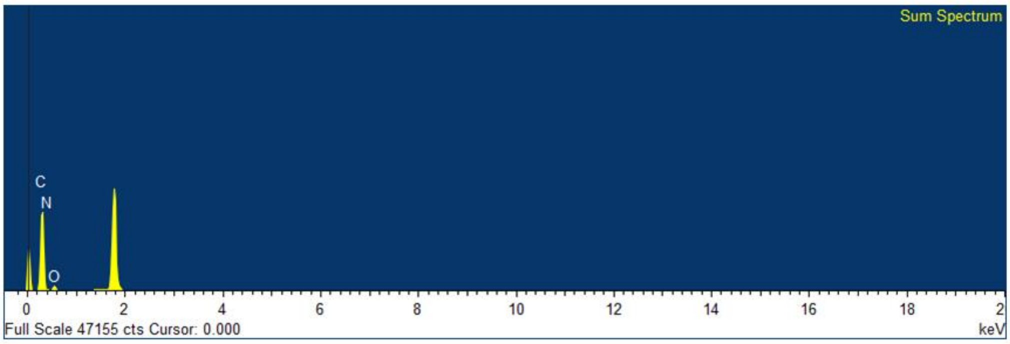

Figure S10. EDX data recorded on **1** showing the different elements present in it.

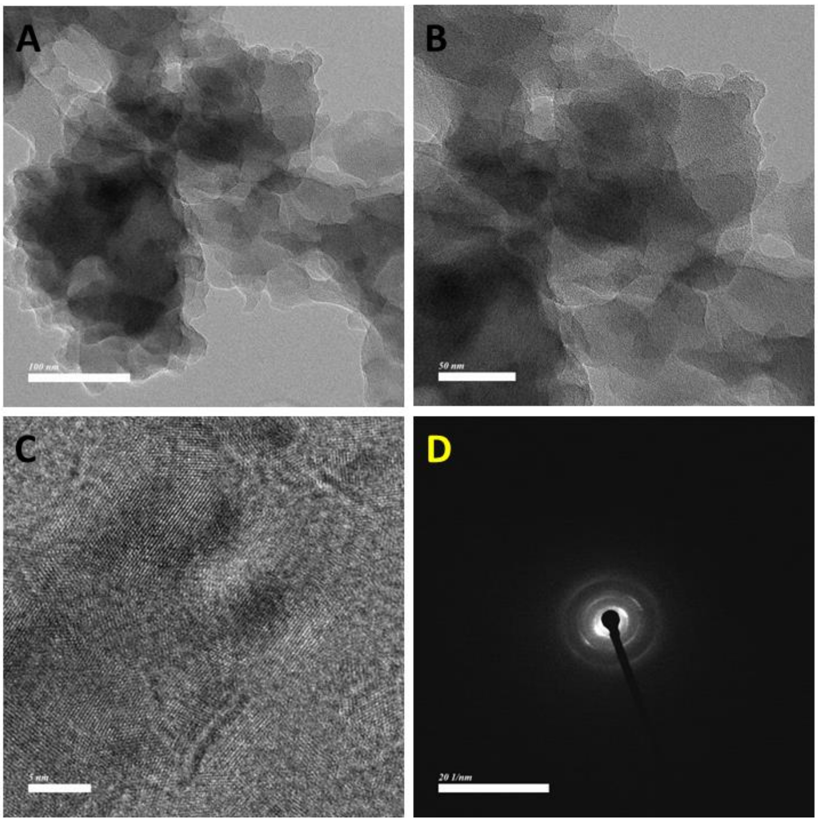

Figure S11. (A,B) HRTEM image of **1** showing the sheet kind structure. (C) Lattice fringes observed in the HRTEM image of **1** showing the crystalline nature of the COF. (D) SAED pattern of **1**.

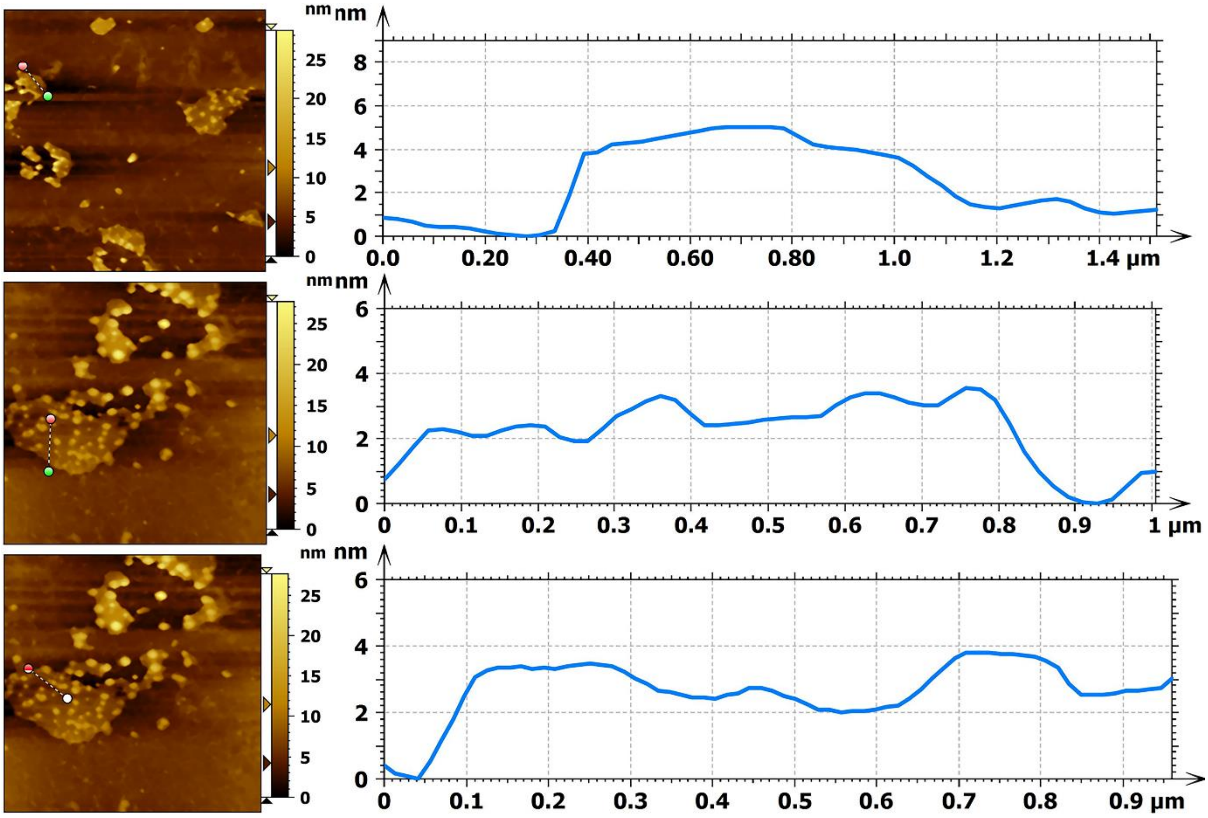

Figure S12: AFM images of the **1** showing the nanosheets character. The average thickness of the covalent organic nanosheets are 4-5 nm.

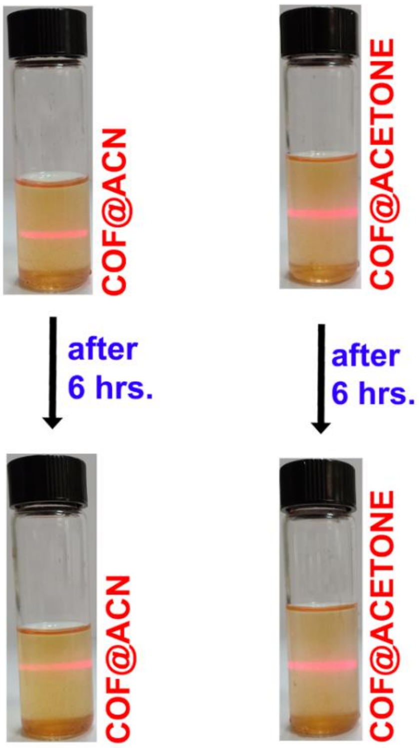

Figure S13. Tyndall effect of the nanosheets dispersed in acetone and acetonitrile (ACN) showing the colloidal stability. The CONs did not settle down even after 6 hours.

Dynamic Light Scattering (DLS) measurements:

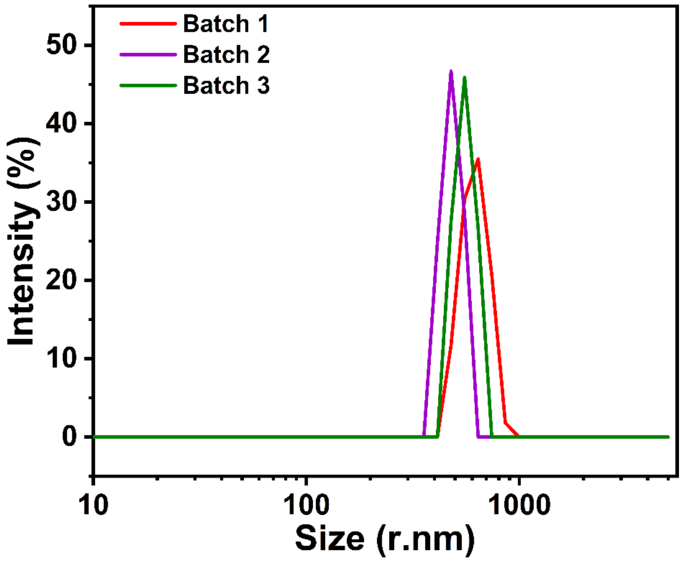

Figure S14. Dynamic Light Scattering (DLS) measurements conducted on three different batches of **1** dispersed in water.

Note: The DLS experment was conducted on three different batch of sample and the resulmts are consistent.

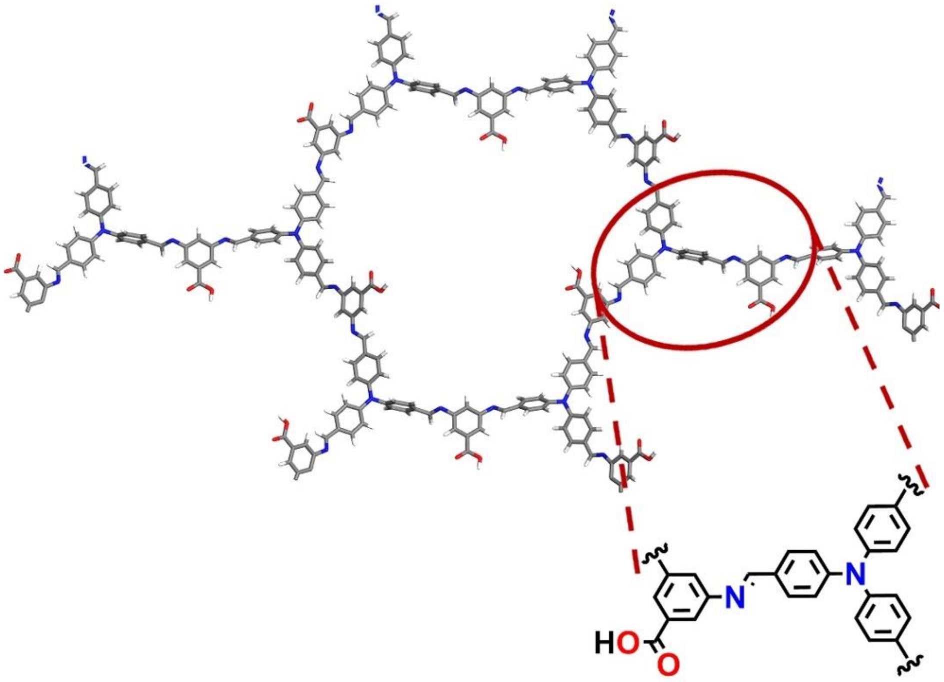

Figure S15. Representation of the single layer of **1** in dry condition showing the buckled layer.

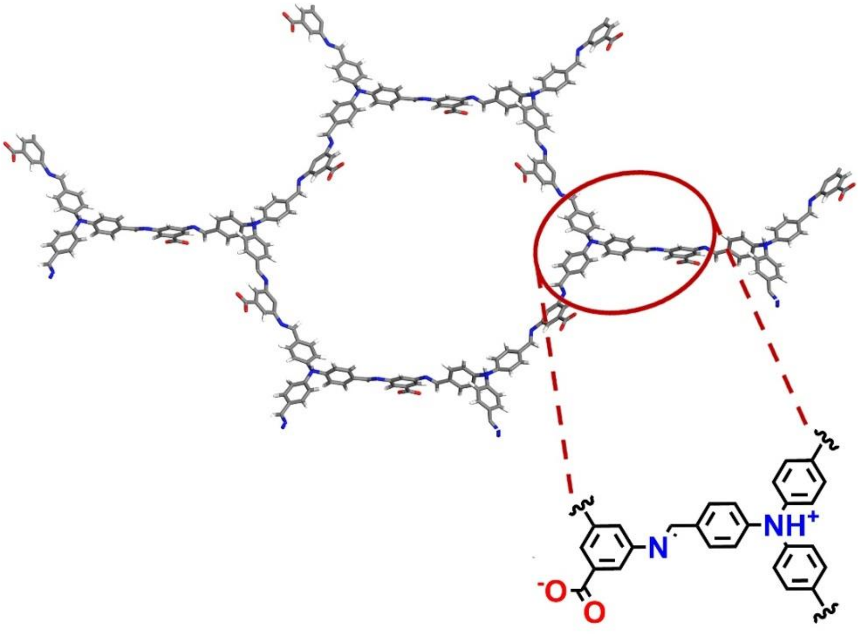

Figure S16. Representation of the single layer of **1** in humid condition showing the buckled layer.

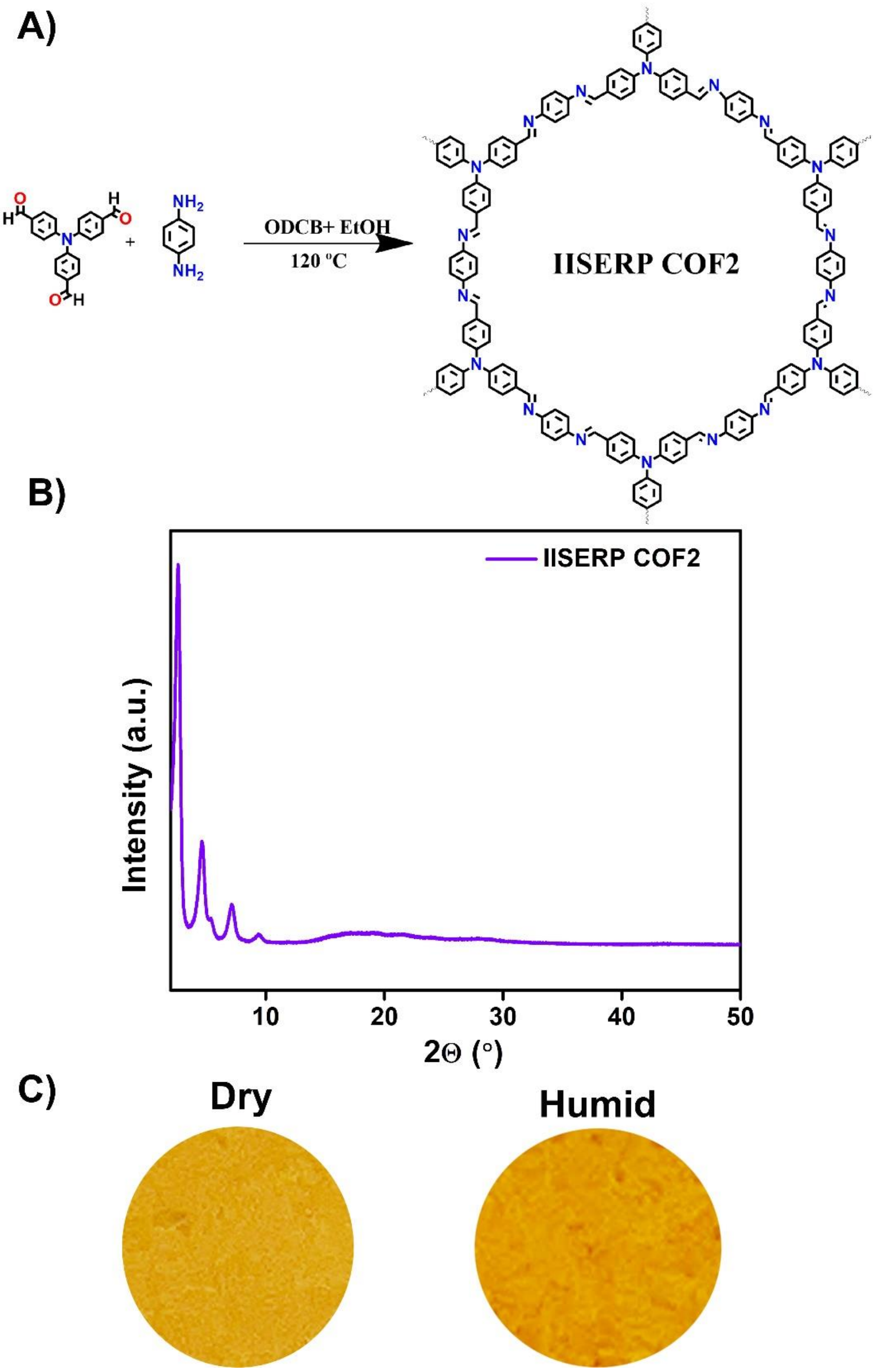

Figure S17. (A) Schematic representation of IISERP-COF2.[S1] (B) PXRD of the IISERP-COF2 which is build from the same aldehyde but the amine does not contain any free -COOH group. (C) Images of the IISERP-COF2 in dry and humid condition.

Note: This COF does not show any humidity dependent color change. This indicate that the presence of COOH group along with the sp^3 *N is necessary for the humidity dependent protonation change which is responsible for the visible color change.*

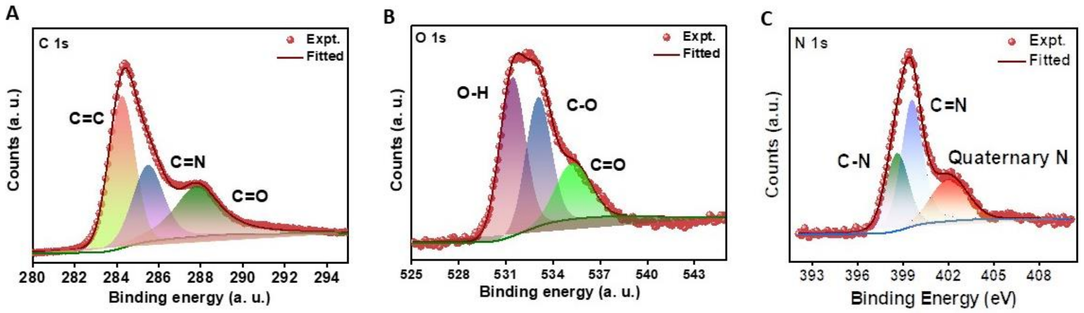

Figure S18. High resolution XPS spectra of **1**. The presence of quaternary N in the N-1s spectra confirms the protonation to the sp^3 N site present in **1**.

5. Spectroscopic studies for humidity sensing:

Photoluminescence studies:

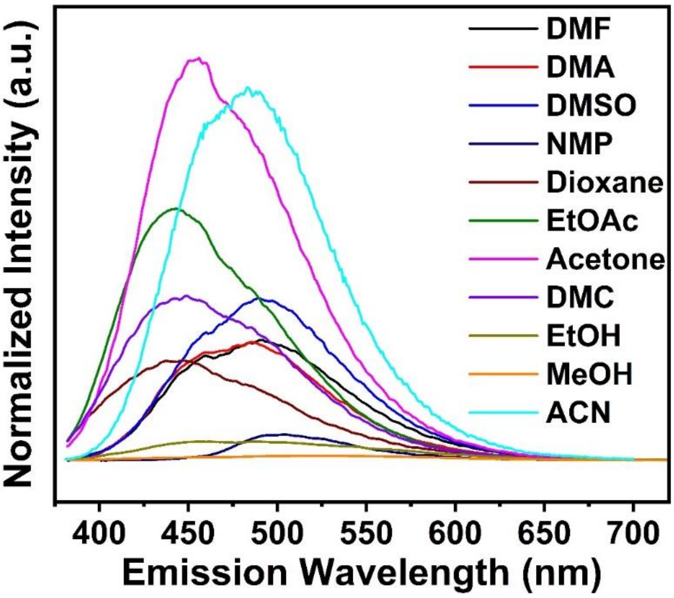

Figure S19. PL emission of the **1** recorded after dispersing in different organic solvents.

Limit of detection calculation:

The limit of detection (LOD) calculation was performed according to the following equation.

Detection limit= (3 σ /k)
where σ = the standard deviation of fluorosence intensity; was measured from the thee blank measurements; k = slope of the Fluoroscence intensity vs concentration of water graph;

In case of acetonitrile, the standard deviation = 1711.812

Blank mesurements	**Fluoroscence Intensity**
1	173900
2	170539
3	172784

Standard deviation	1711.812

Detection limit =(3 x 1711.812)/188935 = 0.027

In case of acetone, the standard deviation = 7968.074

Blank mesurements	**Fluoroscence Intensity**
1	357130
2	350829
3	341303
Standard deviation	7968.074

Detection limit =(3 x 7968.074)/185609 = 0.128

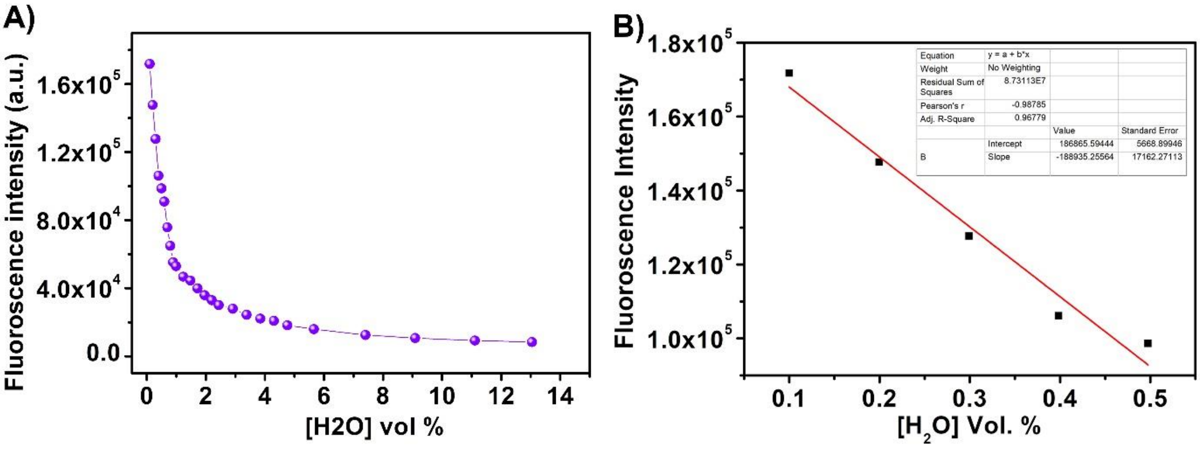

Equation	y = a + b*x		
Weight	No Weighting		
Residual Sum of Squares	8.73113E7		
Pearson's r	-0.98785		
Adj. R-Square	0.96779		
		Value	Standard Error
B	Intercept	186865.59444	5668.89946
	Slope	-188935.25564	17162.27113

Figure S20. (A) Decay in the fluorescence intensity observed as function of increase in the water conc. in acetonitrile. (B) Fluoroscence intensity vs concentration of water (in the low concentartion region) showing the linear fit.

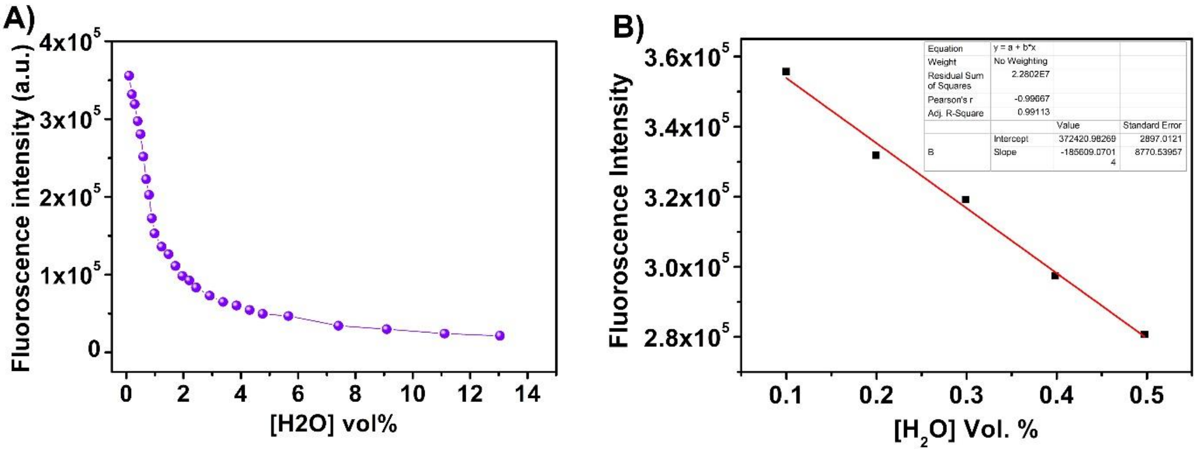

Equation	y = a + b*x		
Weight	No Weighting		
Residual Sum of Squares	2.2802E7		
Pearson's r	-0.99667		
Adj. R-Square	0.99113		
		Value	Standard Error
B	Intercept	372420.98269	2897.0121
	Slope	-185609.07014	8770.53957

Figure S21. (A) Decay in the fluorescence intensity observed as function of increase in the water conc. in acetone. (B) Fluoroscence intensity vs concentration of water (in the low concentartion region) showing the linear fit.

Table S1: Comparison of the sensing performance of various COF and MOF based sensors toward water.

COF/MOF	**Organic solvent where water was detected**	**Min water concentration used for the experiment (%)**	**LOD (%)**	**Reference**
Pythz-COF	ACN/DMF	0.33	0.09/2.94	*Mater. Chem. Front.*, **2021**, 5, 4193–4201
Pyurea-COF	ACN/DMF	0.33	0.02/1.7	*Mater. Chem. Front.*, **2021**, 5, 4193–4201
TAPT-BMTA-COF	ACN	0.33	0.12	*Macromol. Rapid Commun.* 41, **2020**, 2000003
TAPT-TP-COF	ACN	0.33	---	*Macromol. Rapid Commun.* 41, **2020**, 2000003
COF	ACN/DMF/MeOH	1/7/10	0.653/0.262/0.042	*Anal. Chim. Acta.* 1109, **2020**, 114-121
COF TzDa	EtOH	0.4	0.03	*ACS Appl. Mater. Inter*. 9, **2017**, 24999–25005
Carbon Dots	MeOH	10	0.007	*Anal. Chim. Acta.* 1034, **2018**, 144-152
IISERP-COF31	***ACN***	***0.1***	***0.027***	***This work***
IISERP-COF31	***Acetone***	***0.1***	***0.128***	***This work***
$Tb_{97.11}Eu_{2.89}$-L_1	ACN	0.15	0.04	*Chem. Commun.*, **2019**, 55, 6926
LIFM-CL1	MeOH	0.05	---	*Nat Commun* 8, **2017**, 15985.

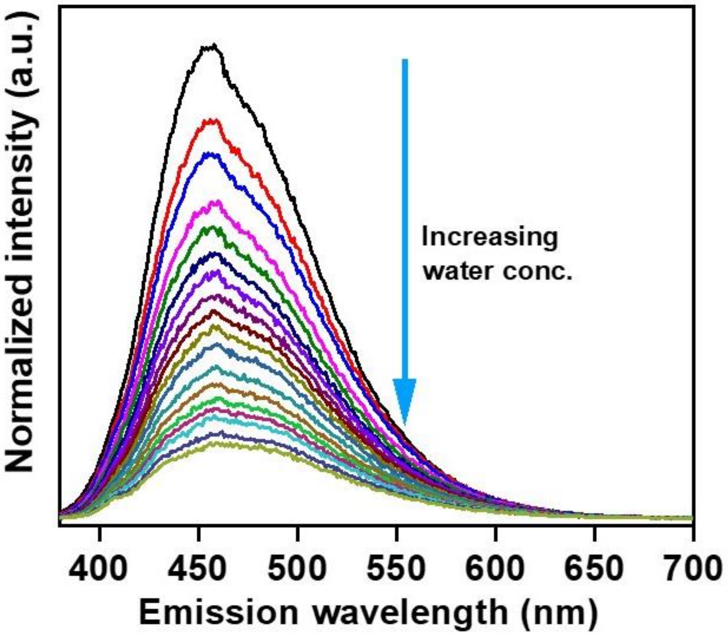

Figure S22. PL Spectra of **1** dispersed in acetone showing the quenching of photo luminescence upon gradual addition of water. Note that the sample is showing exactly same behaviour as presented in figure 5 of main text. This clearly shows the reproducibility of the material for detecting trace water in organic solvent.

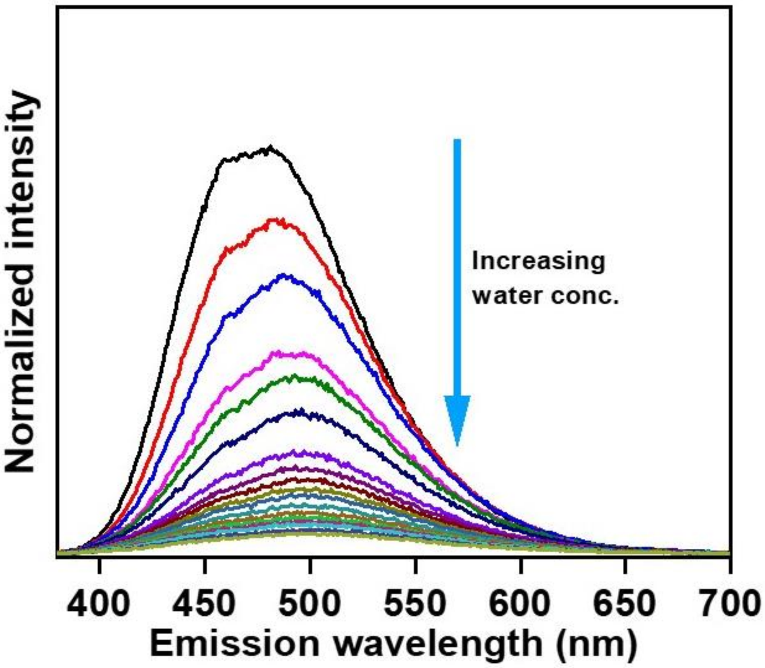

Figure S23. PL Spectra of **1** dispersed in ACN showing the quenching of photo luminescence upon gradual addition of water. Note that the sample is showing exactly same behaviour as presented in figure 5 of main text. This clearly shows the reproducibility of the material for detecting trace water in organic solvent.

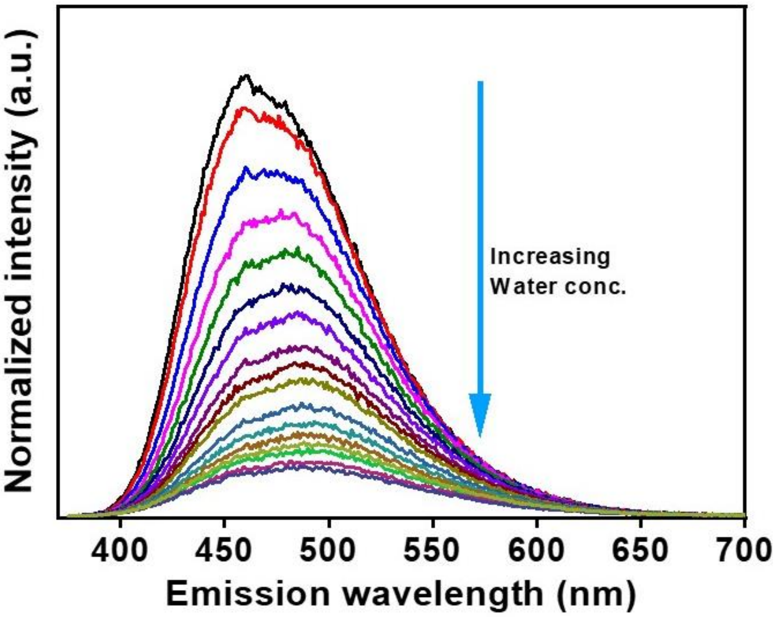

Figure S24. PL Spectra of **1** (after recovering the sample from the 1st cycle) dispersed in acetone showing the quenching of photo luminescence upon gradual addition of water. Note that the sample is showing exactly same behaviour as presented in figure 5 of main text. This clearly shows the recyclability of the material for detecting trace water in organic solvent.

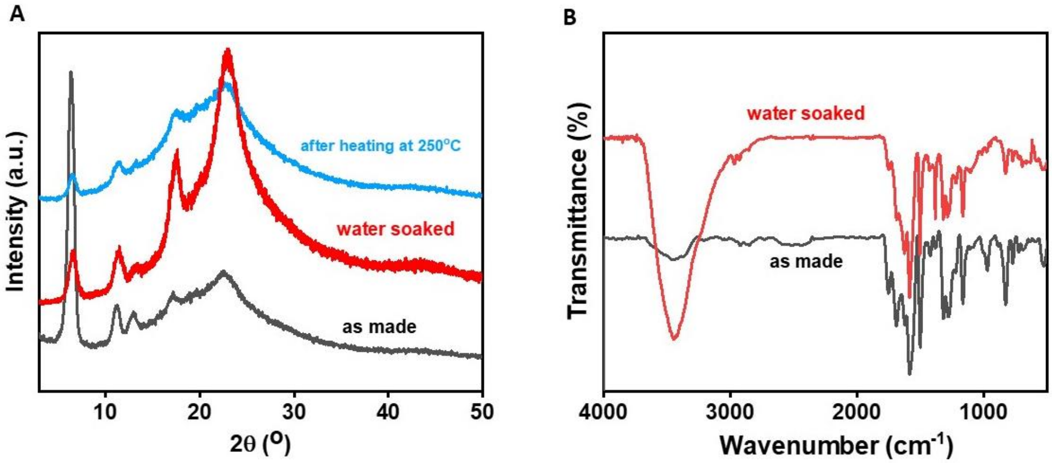

Figure S25. Comparative (A) PXRD and (B) FTIR plot of as made sample vs water soaked sample showing the structural integrity after soaking in water**.** Note: In the PXRD of water soaked sample, the intensity of the (100) peak was decreased and the intensity of the (333) peak was increased compared to as made sample which is a sign of exfoliation. However the FTIR plot shows almost identical vibrational bands (other than a broad peak around 3400 cm^{-1} corresponding to the adsorbed water molecules) which indicates that the structural integrity.

Figure S26. (Left) Photograph of the COF in dry state. (Middle) Photograph of the COF after addition of water droplets.

Note: The red marks in the middle picture are the region where the water drops were added. (Right) Photograph of the COF after drying the wet sample under vacuum.

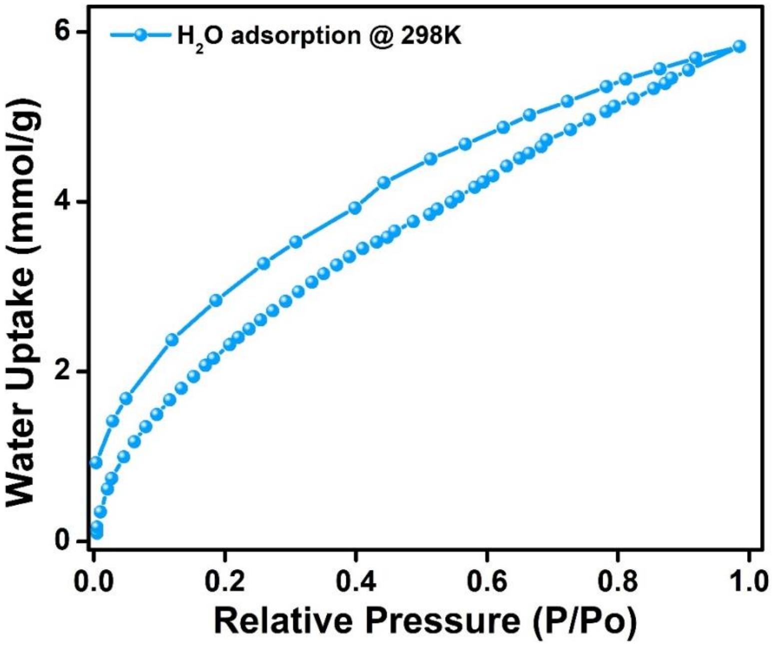

Figure S27. Water sorption isotherm of **1** recorded at 298K. The initial sharp uptake of water indicate strong interaction of water molecule with the framework.

6. Computational details:

DFT/Gaussian calculations All the frontier orbitals related calculation was carried out using a Gaussian-09W program. First the smallest possible model compounds (to restrict the number of atoms for the Gaussian calculations) as presented in figure S28 for dry and humid state was created in the material studio via atomic manipulation. These model compounds were then geometry and energy optimized using a tight binding DFT calculation. These optimized model compounds were then transferred to the Gaussian Software package embedded with Gauss View. The optimized model compounds were then used for the Gaussian calculations (energy optimization) using a DFT/B3LYP method with the 6-311G basis set. The frontier orbitals were extracted from the output of these calculations.

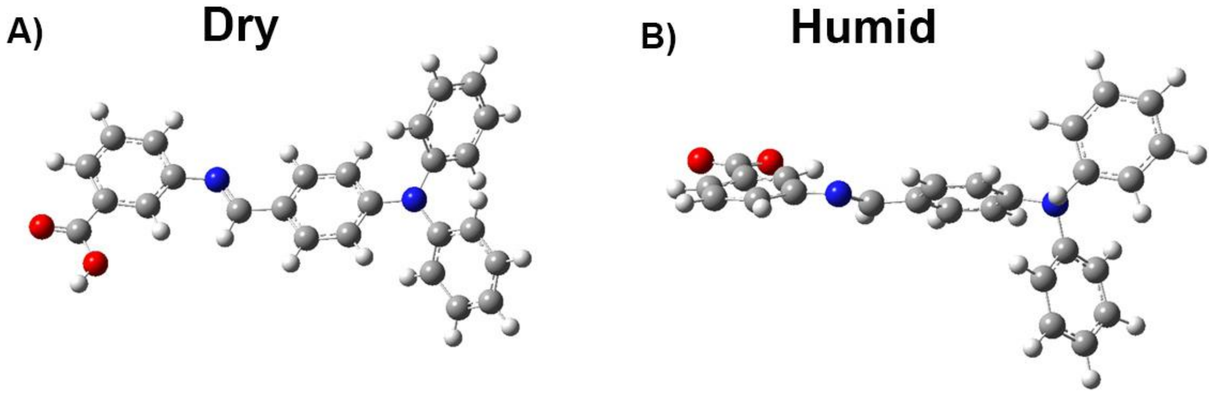

Figure S28. Representation of the model compounds (for dry and humid state) used for the DFT/Gaussian calculations.

Molecular Dynamics simulations of the H_2O and H_3O^+ within the COF - diffusion coefficients and interactions:

A 2 x 2 x 2 cell of the COF with 1 water per unit cell was employed. The initial velocities were made Random. A 50 or 100 ns NPT MD simulation (1.0 fs time step, 300K) was used to generate were used to reach an equilibrium state. The final positions and MSD were determined from the structure subjected to a NVE ensemble (1fs and 100ns). A similar modelling was done consider 6 protonated water molecules per unit cell (one for each *sp*^{3}-nitrogen in the unit cell) which represent the higher concentration of water. Again, we employed the simulated annealing routine to identify the most-favorable position for the H_3O^+ in the COF, which notably turned out to be the same interlayer regions of the COF (spaces in between the *sp*^{3}-nitrogens) as preferred by the single H_3O^+. Again we carried out the MD simulation to see the diffusion coefficient and the RDF plots were used to find if there was a trend in the H_3O^+ residing closer towards the decarboxylated centers and the *sp*^{3} nitrogens. For all teh MD, the Universal force field was employed, and the Coulumbic interactions were treated with Ewald summation methods with a considerable cut-off distance of 15.5 Å, considering the large unit-cell. We did not alter the charge group size. Nose-Hoover Thermostat was employed to control the temperature, while Berendsen barostat helped control the pressure. Energy tolerance of 5×10^5 kcal/mol was applied. Finally, a 100 ns NVE simulations (1.0 fs time step) were used to generate the low-energy trajectory from which we analyzed the radial distribution function (RDF) and the diffusion coefficients were extracted from the slope of the MSD.

References:

S1. Mullangi et al. *Adv. Energy. Mater*. 6, **2016**, 1600110.

S2. Nandi et. al. *Adv. Energy Mater*. **2016**, 1601189.

S3. Chakraborty et. al. *ACS Appl. Mater. Interfaces* **2019**, 11, 15670–15679.